Marshall Plan Scholarship: Final Report

Optical spectroscopy of two-dimensional materials

Visiting Scholar at Massachusetts Institute of Technology, Cambridge, USA
August 21st, 2019 - February 20th, 2020

Lukas Mennel
lukas.mennel@tuwien.ac.at
March 2020

Marshallplan-Jubiläumsstiftung
Austrian Marshall Plan Foundation
Fostering Transatlantic Excellence

Home Institution
Technische Universität Wien
Institute für Photonik
Gußhausstraße 27-29
A-1040 Wien
Thesis Advisor: Thomas Müller

Host Institution
Massachusetts Institute of Technology
Research Laboratory of Electronics
77 Massachusetts Ave
Cambridge, MA 02139
Host Advisor: Dirk Englund

TECHNISCHE
UNIVERSITÄT
WIEN
Vienna University of Technology

Massachusetts
Institute of
Technology

Important notice

Contents

1 Introduction

This document summarizes my work and the obtained results during my visit at the Quantum Photonics Laboratory of Prof. Dirk Englund at the Massachusetts Institute of Technology.
My PhD studies deal with two-dimensional (2D) materials which are a novel class of materials with promising optical, electrical and optoelectronic properties. My research focus lies on the fundamentals of the optoelectronic physics as well as the exploitation of these often exceptional properties to build optoelectronic devices.
The group of Dirk Englund is working with 2D materials as well and they are mainly interested in single photon emitters (SPEs). Optical SPEs form the fundamental building blocks for quantum communication and could also be used for quantum computing. At the moment mostly hexagonal boron nitride (hBN) and tungsten diselenide (WSe_2) are investigated since in those materials quantum light emitters have been observed. However, the nature of these emitters in these materials are not fully understood yet. Nevertheless, it is known that with strain SPEs can be deterministically induced in hBN and WSe_2. In previous experiments Dirks group has used an atomic force microscopy (AFM) tip to strain suspended 2D material flakes locally, however they could not observe any quantum light emission.

My task was to investigate the influence of an conducting AFM tip in proximity to a WSe_2 monolayer. In order to study this influence we fabricated samples, which allow full electric control and simultaneous optical probing, we built an experimental setup, and we conducted the measurements.

This report is structured as follows. The fist chapter describes the optoelectronic fundamentals of 2D materials. Next, the experimental setup and the sample fabrication process are explained. Then, the experimental results are presented and discussed. Finally, we summarize the results and an outlook for possible follow up studies is given.

2 Fundamentals

2.1 Two-dimensional material optoelectronics

Two-dimensional (2D) materials exhibit many unusual physical properties, compared to conventional bulky materials. The confinement and the weak dielectric screening of the electrons to only two dimensions gives rise to exceptional electron-hole interactions which form so called excitons with binding energies of tens of electron volts.[1] These tightly bound excitons dominate the optical response even at room-temperature. Another optoelectronic characteristic of TMDs is the large spin-orbit coupling which is connected to circular dichroism. This results in a spin- and valley-selective excitation of excitons. Right-hand and left-hand circularly polarized photons induce K or K' valley optical transitions only[2–6]. There are different types of excitons, including optically allowed (bright) and optically forbidden (dark) excitons. The dark excitons can be divided into momentum and spin forbidden dark excitons. The momentum forbidden dark exciton consists of a coulomb bound electron hole pair where the electron and hole are located in different valleys. This implies that for an optical transition a phonon is needed to fulfill momentum conservation. In TMDs there is a strong spin-orbit interaction which lifts the spin degeneracy for the conduction and valence bands. In the conduction band, the sign of tungsten- and molybdenum-based TMDs, is different. Therefore, in MoS_2 and $MoSe_2$ spin allowed bright excitons is the lowest energy state while in WS_2 and WSe_2 the spin forbidden states have the lowest energy[7]. With magnetic fields, the dark spin forbidden dark excitons can be brightened in WS_2 and WSe_2[8,9]. The orientation of the dipole moment is intimately linked to other properties of the excitons. Dark excitons have a non-zero out-of-plane dipole moment while dipole moment of the bright excitons lies within the 2D plane[10]. Therefore, high numerical aperture (NA) objectives are needed to observe dark excitonic transitions. Since in the course of this work we did not use a high NA objectives we did not see such excitons.

In realistic samples there is always some strain present and also impurities which can trap electrons and holes in their potentials which results in localized excitons. These localized excitons can only be observed at low temperatures. At room temperature the potential wells are too shallow to trap charge carriers and therefore no localized excitons can be observed. It has been shown that these localized excitons are the source of single-photon emission from TMD monolayers. These localized emitters can be deterministically induced with strain and are often observed at edges of TMD flakes[11–15]. The spectral linewidth of the emission can be below 120 ueV in a free standing WSe_2 monolayer.[11] Such emitters would be useful in many potential applications but the SPEs in TMDs are not yet fully understood.

For WSe_2, which is in focus of this study, the binding energy of the free bright exciton is 0.37 eV on a SiO_2/Si substrate.[16] Excitons are bosonic particles and therefore only populate the lowest energy state when the system is in the ground state. The Bohr radius of the exciton is directly connected to its effective mass which is, compared to other semiconducting materials like GaAs or InAs, rather small. In WSe_2 the exciton Bohr radius is around $10-20$ Å, and therefore the excitons in TMDs are called tightly bound.[17] The effective mass is give by the inverse of second derivative of the Energy in respect to the wavevector, or in other words by the inverse of the curvature of the electronic bands. For excitons in TMDs this is the curvature at the K and K' point in momentum space. By means of engineering the Bohr radius of excitons in 2D materials could only easily be influenced by the dielectric environment of 2D crystal.

Excitonic complexes with more than two particles are expected to have bigger Bohr radii[18,19]. In fact there are a multitude of multi-particle exciton complexes in 2D materials. Three particle states, called trions[18,20,21], can either be positively charged when two holes interact with an electron, or negatively charged when a single hole is interacting with two electrons. Like the exciton, a trion can also be dark or bright, depending on the involved valleys which are hosting the electrons and holes.

Also four- and five-particle states are observed in WSe_2[21–23], which are called neutral biexcitons and charged biexcitons. A neutral biexciton consists of two electrons and two holes and is therefore charge neutral. The charged biexciton can be positively or negatively charged, depending if there is an additional hole or electron interacting with a neutral biexciton. In 2D materials it is possible to significantly influence the carrier density by electrostatic gating, which is commonly done with a back gate. By applying a positive (negative) potential to the back gate it is then possible to increase (decrease) negatively/positively charged exciton complexes such as the negative/positive trion and the negatively/positively charged biexciton.

In order to identify which peaks of the PL emission spectrum corresponds to which exciton complex, fluence dependent PL measurements are used for identification. In full thermal equilibrium (neglecting any possible increase in temperature with rising laser intensity) there would for example be a quadratic relation between exciton (X) and biexciton (XX) density $I_{XX} \propto I_X^\alpha$ with $\alpha = 2$.[24] However, due to a lack of equilibrium between the states, the experimentally observed exponents lie between 1.2 and 1.9[19,25,26]. Nevertheless, the exponent scales with the number of particles in the exciton complex and is therefore a strong indicator. Besides fluence measurements, also valley coherence measurements can give insights into the nature of the exciton complex which gives rise to a certain PL emission.

Trions excited by linearly polarized light have three possible configurations of placing the electrons and holes in the two valleys and due its nonzero charge there is fine structure between those states. This coulomb exchange splitting destroys the valley coherence. Therefore, trions excited by linearly polarized light are subject to valley pure dephasing which destroys the coherence.[27,28] This is not the case for excitonic complexes with zero charge. Also when the 2D crystal is excited with circularly polarized light, the valley coherence is not affected by the net charge of the excitonic complex. In short, this means that polarization dependent measurements can also be used to characterize PL emission peaks.

2.2 Band bending

Band bending is the effect when in semiconductors the bands in the band structure are bent at junctions, which could for a example be a p-n semiconductor junction or a metal-semiconductor interface (Schottky barrier). This band bending happens due to a local imbalance in charge neutrality, which is also known as a space charge. Such a charge imbalance can not only be induced at junctions but are also induced electrostatically. For example in scanning tunneling microscopy (STM) of semiconductors, the observed barrier height, which is obtained from the tunneling current, can be much lower than the real barrier height.[29] This is because the electrostatic field of the STM tip causes a local bend bending in the device and a lowering of the tunneling barrier and must be compensated for in STM measurements of semiconductors. This STM tip induced band bending has been used to create qunatum dots (QDs) in indium arsenide (InAs)[30] and gallium arsenide (GaAs)[31]. These tip induced quantum dots have been investigated electrically[30] as well as optically[31]. In the electrical measurements the quantum dot energy levels can be observed in the dI/dV curves. They saw two quantization levels in z direction and ladder of quantization levels in lateral direction. They were able to reconstruct the band bending potential by analyzing the tip induced states. In the optical study of the tip induced QD in GaAs, they observed STM-induced luminescence spectra of the QD and were described the voltage and current dependence of the luminescence peaks. Due to the many body nature of the interactions they were not able to formulate an accurate description of their system.

In both studies they used materials with very low effective mass electrons and holes. In GaAs the effective mass of the exciton is about and in InAs the effective mass is even. The small effective mass leads to big Bohr radii of the excitons, 14.9 nm and 51.6 nm for GaAs and InAs respectively[32,33].

Which makes the exciton Bohr radius in these materials an order of magnitude larger than of the excitons observed in semiconducting atomically thin crystals. This is important because the relative length scale of the wavefunction and the quantum dot determine the nature of the interaction. If the wavefunction of the exciton is larger than the potential of the quantum dot, the weak confinement regime, then coulomb interactions dominate. If however the exciton wavefunction is larger than the potential it is trapped in then we are in the strong confinement regime and the physics is dominated by the geometry of the quantum dot.[34] In the strong confinement regime there are exciton complexes with more particles observable which are unstable when they are in higher dimension semiconductors. From this viewpoint, atomically thin crystals can be seen as quantum wells which are strongly confined in one dimension. In the following investigation we are exploring what happens when we confine the excitons in 2D materials also laterally by band bending using an electrically charged AFM tip.

3 Experimental setup

The experimental setup can be split into three parts: optics, AFM tip control, and cryogenics. The schematic drawing of the experiment is shown in Figure 1. A van der Waals (vdW) 2D material stack is placed on top of a transparent substrate (microscope coverglass) which is placed upside down and optically probed from the backside. A conductive AFM tip is placed underneath the sample and can be brought into contact with the vdW 2D material stack. The experiment gives us control over the following variables: x-y position of the AFM tip, sample-AFM tip distance, electrical potential of the AFM tip (V_{tip}), the backgate voltage which controls the charge carrier density of the sample ($V_{backgate}$), and the energy, intensity, polarization of the excitation laser.

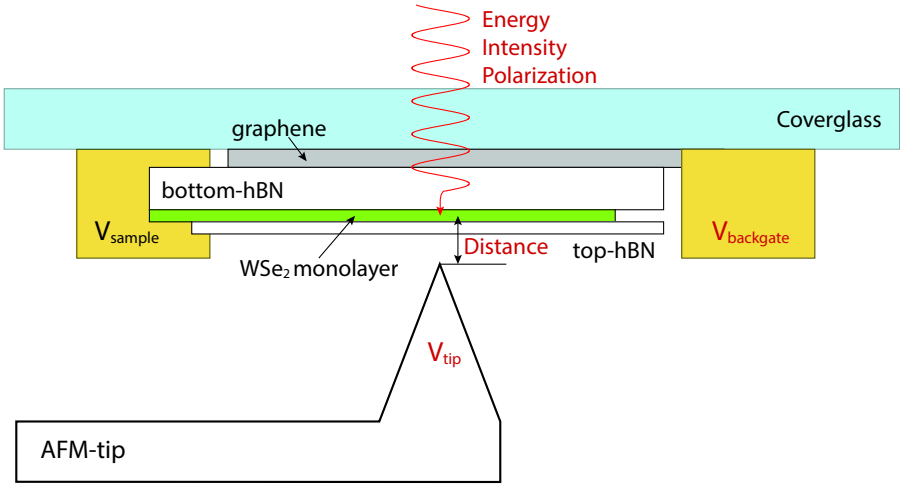

Figure 1: Schematic drawing of the experiment. The van der Waals 2D material stack is hosted on a microscope coverglass which allows optical probing with a laser from the top. A graphene layer functions as a backgate. Bottom- and top-hBN encapsulate the WSe_2 monolayer and functions as an isolating dielectric. A conduction AFM-tip can be freely moved in x, y and z dimension and be placed close to the WSe_2 monolayer.

3.1 Optics

In the course of our experimental investigation we used three different excitation lasers. First a laser diode (533 nm), second a HeNe laser (633 nm) and third a tunable narrow-band (< 1 MHz) laser M2 SolsTiS EMM laser system. The laser diode was only used for alignment purposes and to obtain reflection images. The HeNe laser was used for most of the experiments. The tunable laser system was used for the photoluminescence excitation (PLE) measurements where we sweeped the excitation energy. Since the intensity of the laser depends on the emission wavelength we monitor the power before the objective and compensate this influence for these measurements. If not indicated otherwise, we used a laser intensity of ~ 3 uW which was focused onto the sample with a 100x objective which corresponds to a fluence of $\sim 10\,\mathrm{uW/um^2}$. Furthermore, we used circularly polarized excitation light and only did polarization filtering of the optical response if it is specifically noted. To scan the laser across the sample we used a Galvo mirror system, which consist of two mirrors mounted on two Galvanometers which deflect the light in x and y direction. The photoluminescence spectra were recorded with a IsoPlane SCT 320 spectrometer

from Princeton Instrument. Emission counts were measured with APD modules from Excelitas (SPCM-AQRH).

3.2 AFM tip control

In Figure 3, the AFM tip holder can be seen, which hosts the nanoscale AFM tip and connects it to the scanning and stepping piezo stages for the positioning (Attocube Inc.). The AFM tip was glued under a small angle onto the AFM tip holder with silver paint. Placing the AFM cantilver under an small angle ensures that only the tip comes into contact with the sample. The AFM tip is electrically connected to the AFM cantilever which itself is electrically connected via bonding wires. The electrical potential of the AFM tip is controlled with a source meter (Keithley). By using the laser scanning system we are able to locate the exact position of the AFM tip and are also able to determine its distance to the sample. By exploiting the laser reflection we are able to convert the voltages of the piezo scanners to a position in space. Scanning electron microscopy (SEM) images of the AFM cantilever and the tip are presented in Figure 2

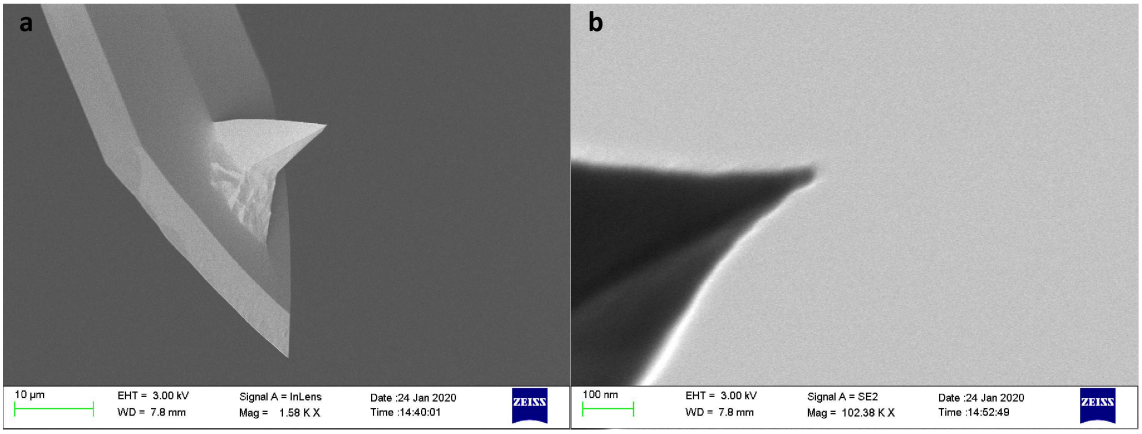

Figure 2: SEM images of the AFM tip. **a**, Overview image of the AFM cantilever with the tip on top. The tip and cantilever are in electrical connection. **b**, Close up image of the AFM tip. The AFM tip radius is below 30 nm.

3.3 Cryogenics

We used a closed-cycle cryostat from Montana Instruments at T= 4 K to perform low temperature measurements. The open cryosate chamber can be seen in Figure 3. In this Figure the cold fingers are labeled which are cooled down. We connected both of those fingers with a sample holder made out of copper. On this sample holder we mounted a printed circuit board (PCB) which has a 4 mm thick aluminum core. The aluminum core is in direct contact with the copper sample holder which ensures a good thermal coupling. Underneath the PCB we placed our actual sample which has a transparent substrate (microscope cover glass). The sample on the coverglass is placed directly under the hole of the PCB which allows optical probing from the backside of the sample. The electrical contacts on the sample are wire bonded to the PCB and connected to a second source meter (Keithley). The pressure inside the cryostat was below 10^{-6} mbar during the measurements.

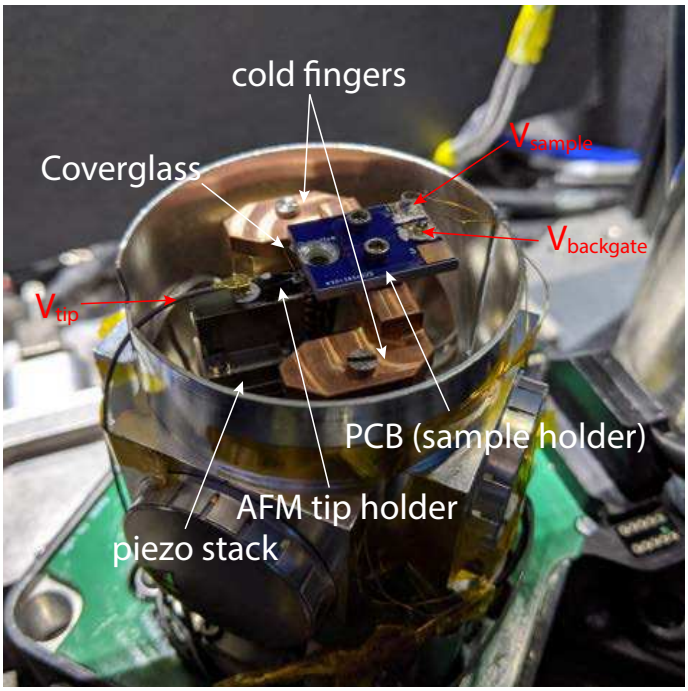

Figure 3: Inside of the Montana cryostation. The microscope coverglass with the 2D material stack is mounted on a aluminum core printed circuit board (PCB) which is mounted to the cold fingers with a copper holder. The conducting AFM-tip is mounted on a AFM-tip holder which is placed on a piezo stack. There are three electrical connections: electrical potential at the AFM tip (V_{tip}), WSe_2 monolayer (V_{sample}), and graphene flake ($V_{backgate}$).

4 Sample fabrication

We mechanically exfoliated WSe_2, hBN and graphene on SiO_2/Si substrates. We used substrates 280 nm thick SiO_2 for WSe_2 and graphene, and 90 nm thick SiO_2 for hBN. Because the optical contrast of thin hBN flakes is more pronounced on 90 nm thick SiO_2.[35] Then we used polycarbonate (PC) covered (PDMS) stamps to pick and place the individual flakes onto a transparent microscope coverglass substrate. In Figure 1 the upside down view of the fabricated vdW 2D material stack can be seen. A graphene flake is on the bottom and covered by a thin bottom-hBN flake. Followed by a WSe_2 monolayer which is then covered by a very thin top-hBN flake.

Next we used optical lithography (Heidelberg Laser Writer) to write two electrodes which connect the WSe_2 flake and the graphene which is functioning as a backgate. Then we evaporated 3 nm Ti and 30 nm Au. In Subfigure 4a overview and a close up view microscope images of the sample. The concentric rings are functioning as a visual guidance for the correct placement of the sample on the PCB. In close-up microscope image the placement of the individual flakes are indicated by dashed lines and show how the actual vdW stack looks.

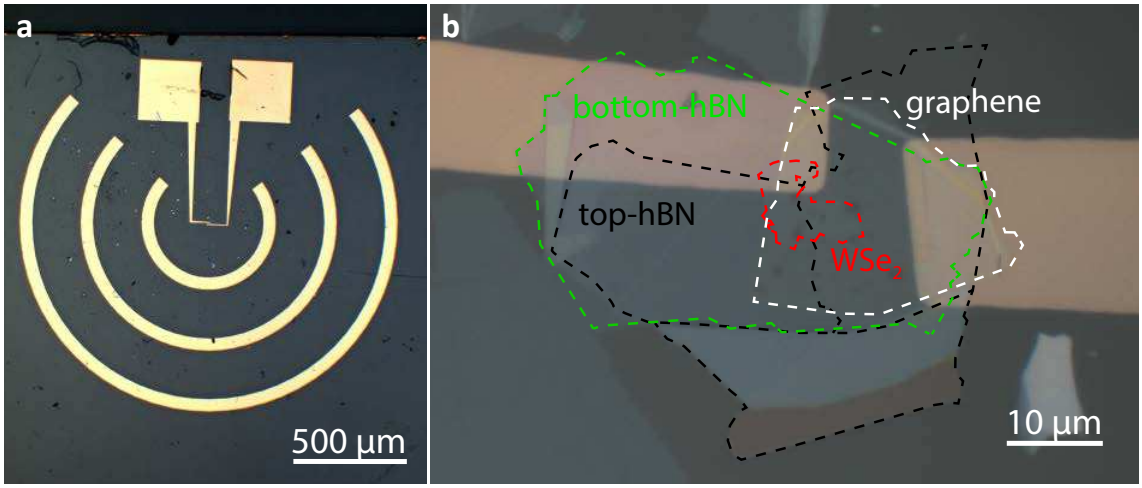

Figure 4: Microscope images of the 2D material stack on top of cover glass, with lithographically defined gold structures. **a**a Overview image where the bonding pads on the top and the concentric alignment rings can be seen. **b**a Close up view of the vdW stack. The ordering is as follows: microscope cover glass, graphene, bottom-hBN, WSe_2 monolayer, top-hBN, gold electrodes. The left-hand side electrode is connected to the WSe_2 monolayer and the right-hand side Au electrode is connected to the graphene, which functions as a electrostatic backgate. The dashed lines indicate the outlines of the 2D crystals.

In Figure 5 laser reflection images of the sample is shown when the sample is mounted in the cryostat. On the left-hand side the vdW stack and the gold electrodes can be seen. On the right-hand is the laser reflection image of the AFM cantilever which is placed below the vdW stack. The dark rhombus inside the cantilever reflection shows the bottom of the AFM tip. The top of the AFM tip is not exactly in the middle of the bottom rhomboidal outline. From the SEM images we extracted the exact tip location in relation to the rhomboidal bottom outline of the tip. With this information we were able to place the tip exactly (with sub-micrometer accuracy) to a desired position on the WSe_2 flake.

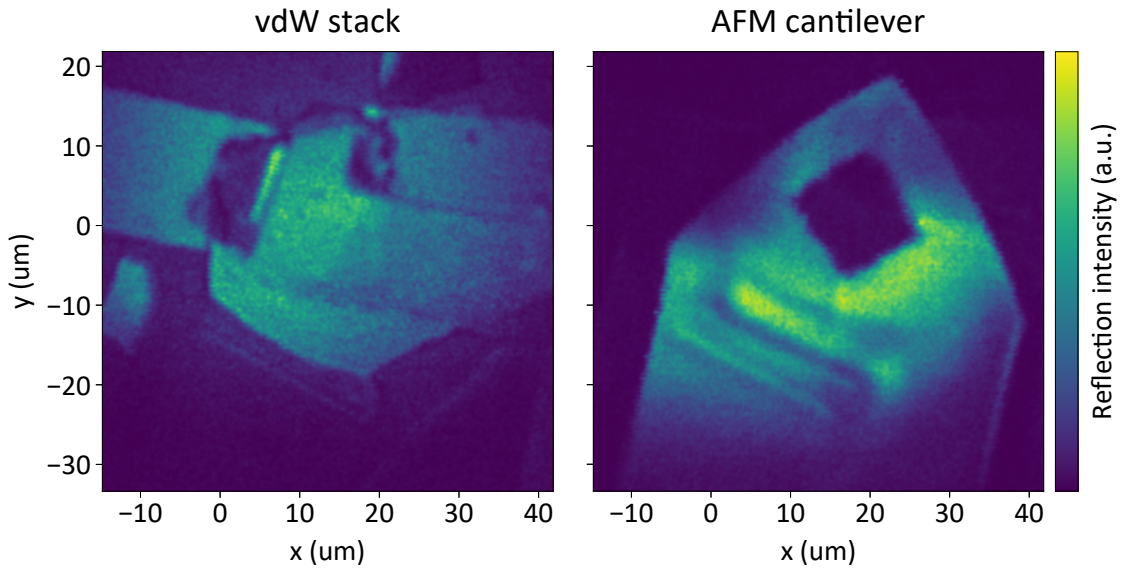

Figure 5: Laser reflection images. Left-hand side: Image of the van der Waals 2D material stack mounted in the Cryostation. Right-hand side: Image of the AFM cantilever which is below the van der Waals 2D material stack. The shadow of the gold contacts at the top and the thick hBN part at the bottom can be seen.

5 Results and discussion

In Figure 6 the PL intensity maps of the WSe_2 flake is shown. Here, the AFM tip is in contact with the sample at position: x = 18.3 um, y = 1 um. In Figure 6a, the tip potential (relative to the WSe_2 flake) is set to V_{tip}= 0 V. When the tip voltage is turned on (to V_{tip}= 10 V) a new optical feature in the PL map is appearing, at the location where the AFM tip is placed, see Figure 6b. The PL spectrum of this feature, when the tip is turned on and off, is in Figure 6c. When the tip voltage is at 0 V the typical spectral features like exciton, trion and localized exciton emissions are visible. However, when the tip voltage is set to 10 V then these typical spectral features disappear at this position and a new peak at 1.67 eV appears which is much stronger than the typically observed light emission. Note that in Figure 6c the curve with Vtip = 0 V is enlarged by a factor of 10, relative to the spectrum with Vtip = 10 V.

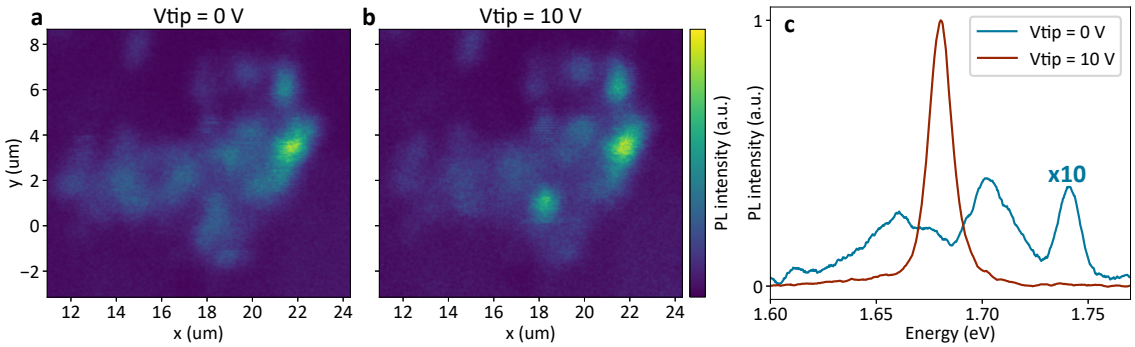

Figure 6: AFM tip in contact with the sample. **a**, PL map with AFM tip at 0 V. **b**, PL map with AFM tip at 10 V. **c**, PL spectras with at the tip location for the two different tip voltages. Both the backgate and WSe_2 voltage is at 0 V.

5.1 Electrical tunability

Let us first investigate the electrical tunability of this charged AFM tip induced emission. From the first measurements in Figure 6 we know that we can control the localized emission with the tip voltage (V_{tip}). In Figure 7b a colormap of PL spectra for varying tip voltages and a fixed backgate voltage (V_{bg}= 0 V) is shown. When the tip voltage is at zero we can see a typical spectra which shows exciton, trion and localized exciton lines, which can be found at any location on the sample. However, if the tip voltage changes to the positive, first, at around 5 V, the trion line becomes more pronounced and the exciton lines diminishes. This shows that at the tip location the carrier concentration changes and that more electrons are accumulated in this area. If we increase the tip voltage further, then a novel spectral feature appears and all other spectral features like exciton, trions, and localized exciton peaks are diminishing.

When we compare the PL colormaps for different backgate voltages we can see that for a positive backgate voltage (Figure 7a) the localized peak emission starts is setting in for lower tip voltages. For a negative backgate voltage (Figure 7b) the localized peak emission is only forming for higher tip voltages. As soon as the tip induced emission has formed, further increasing the tip voltage does not change the energy nor the intensity of the emission as can be seen in Figure 7a. For a V_{bg} of 1 V, 0 V, and −1 V the localized peak gets visible for a V_{tip} of $\sim$ 2.5 V, $\sim$ 5 V, and $\sim$ 7.5 V. Which means that the carrier concentrations in the WSe_2 flake plays a key role in

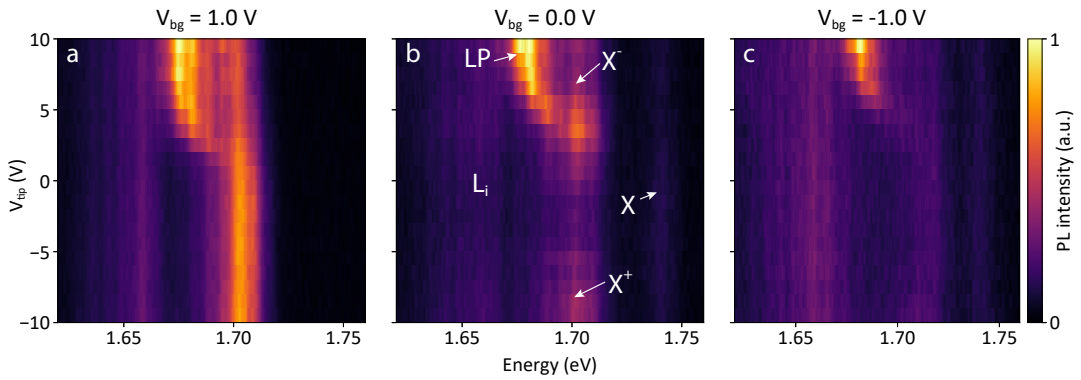

Figure 7: Colormaps of the PL spectra as a function of the AFM tip voltage (V_{tip}) for different backgate voltages: **a**, V_{bg}= 1.0 V; **b**, V_{bg}= 0.0 V; **c**, V_{bg}= −1.0 V. In **b**, the different peaks are labeld: LP: localized peak; X: exciton; X^+: positive trion; X^-: negative trion; L_i: localized excitons.

the nature of this new localized PL peak. Furthermore, the energy of the localized peak emission seems to change with the backgate voltage.

In Figure 8 we sweep the backgate voltage while keeping the tip voltage constant at V_{tip}= 10 V. In Figure 8a the PL spectra are shown in form of a colormap and in Figure 8b some of the PL spectra are plotted. The localized peak is fitted with an Lorentzian

$$\text{Intensity} = I \times \frac{\gamma^2}{\gamma^2 + (x - x_0)^2} \tag{1}$$

and the fitted parameters are shown in Figures 7c-d. 7c shows the relative peak position (relative to backgate voltage V_{bg}= −2.5 V) which correlates with the backgate potential. For positive backgate voltages it shows a linear dependency while on for negative backgate voltage values the correlation seems to be more complicated. In the positive backgate voltage regime the gradient of the peak position (x_0) to backgate voltage has a value of $\nabla_{x_0} = -2.73 \pm 0.1$ meV/V. The relative peak height $I_{rel} = I/I(V_{bg} = 2.5\,V)$ depends on the backgate voltage as well and changes with $\nabla_{I_{rel}} = 0.066 \pm 0.005\,V^{-1}$. Below a backgate voltage V_{bg}= −2 V the tip induced peak disappears. This behaviour is in line with the previous measurements (see Figure 7) and that gives a electronic condition for the formation of the tip induced emission

$$\frac{V_{tip} - 5\,V}{V_{bg}} > 2.5. \tag{2}$$

In contrast to peak position and height, the peak width is constant (the fitted gradient is $\nabla_{I_{rel}} = -0.02 \pm 0.09$ meV/V) and has a value of 5.4 meV. Which means that the carrier lifetime is unaffected by the density of carriers. Only when the transition in the PL spectra from localized peak to free excitonic particles is happening, the linewidth of the tip induced peak is broadening and the peak height is going down quickly (see Figure 8c and 8d for backgate voltages below −2 V).

5.2 Excitation control

Here we investigate the dependence of the tip induced localized emission on the excitation. The tip is kept at V_{tip}= 10 V and the backgate at V_{bg}= 0 V. In our excitation investigation we consider

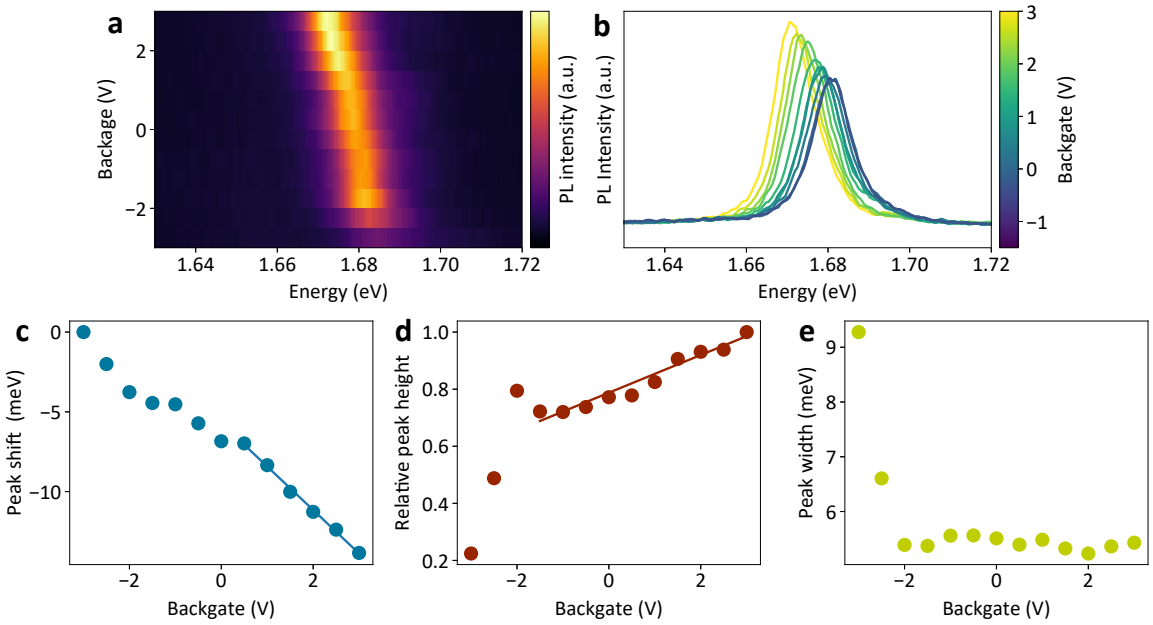

Figure 8: Control of the localized PL emission with the backgate. The tip voltage is at V_{tip}= 10 V for all measurements. **a** Colormap of the PL spectra plotted as a function of the backgate voltage. **b** PL spectras for backgate voltages above −2 V. **c-e** Relative peak shift, relative peak height and peak width of the localized emission as a function of the backgate. These values are obtained by fitting the PL spectra with a Lorentzian funciton.

the polarization, energy, and fluence dependence. First, we look at the polarization dependence and for that we use circularly (left-handed) polarized light with a wavelength of 633 nm and with 3 uW power. In Figure 9a we see the PL spectra where we collect only the left-handed polarization (co-polarized configuration) and the right-handed polarization (cross-polarized) and we can see that the intensity depends on the polarization filtering. To quantify this we use a metric called degree of polarization (DOP) which is defined as

$$\mathrm{DOP} = \frac{I_{\mathrm{co-pol}} - I_{\mathrm{cross-pol}}}{I_{\mathrm{co-pol}} + I_{\mathrm{cross-pol}}}. \tag{3}$$

For circular polarization we get DOP= 0.37 which shows the valley coherence of tip induced peak under this excitation. For linearly polarized light, which is illustrated in Figure 9b, we get of basically DOP= 0 (the slightly lower intensity of the VH configuration comes from the additional absorption of the $\lambda/2$ plate which is in the optical path in this configuration. Under linearly polarized light excitation no valley-coherence is observable. This is the same behaviour which is shown by a trion and is in contrast to the behaviour of an exciton.[27,28] Since the valley coherence is destroyed when linearly polarized but not when circularly polarized, this strongly indicates that a coulomb interaction is part of this interaction. This means that the exciton complex which gives is involved in this localized peak emission must be charged and therefore can only be a trion or another charged excitonic complex of higher order.

In Figure 9c we present the PLE result. We used the M2 SolsTiS EMM laser system to tune the wavelength. Since the laser power is depending on the emission wavelength we monitor the laser power and normalize the PL intensity. In this measurement we used a APD to collect the

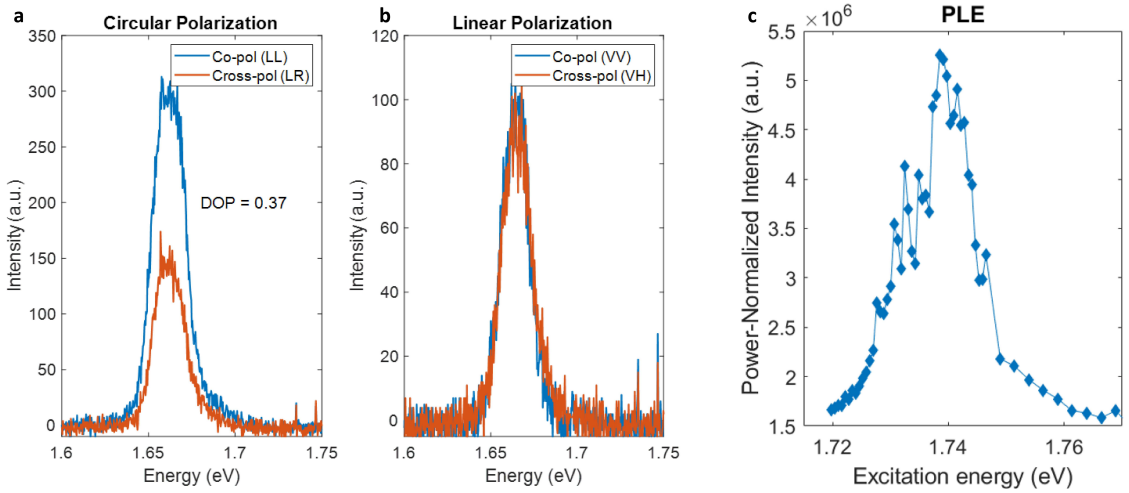

Figure 9: Polarization dependent response of the localized PL emission. **a**, Circularly polarized laser excitation and circular filter before the spectrometer. LL stands for left-handed excitation and left-handed filtering before detection - co-polarized configuration. LR stands for left-handed excitation and right-handed filtering before the spectrometer, which is the cross-polarization configuration. **b**, V stands for linear vertical polarization and H stands for linearly horizontally polarized light. VV is the co-polarized configuration and VH is the cross-polarized arrangement. **c**, Photoluminesence excitation (PLE) measurement. The power normalized integrated PL intensity depending on the excitation laser energy is shown. A clear resonance around the free exciton energy ($\sim 1.74\,\mathrm{eV}$) is visible.

signal and we used spectral filters to only measure the localized peak emission. A strong resonance is visible in the 1.72 eV to 1.75 eV range which coincides with the exciton energy which we know from the PL spectra we took in Figure 7. The PL efficiency of the tip induced emission is increased by a factor of ~ 3.3 when excited resonantly with the exciton.

The final investigation regarding the excitation was the change of the optical power. Till now we kept the excitation intensity at $\sim$ 3 uW which corresponds to a fluence of $\sim 10\,\mathrm{uW/um^2}$. Here, we vary the intensity which and track the exciton, negative trion, and the tip induced PL peak. The tip volatage is kept at $V_{tip}= 10\,V$ and the backgate at $V_{bg}= 0\,V$. In Figure 10 the measurements are shown. Usually (without an electrically charged tip in proximity of the WSe_2 flake), the exciton peak scales linearly with the excitation power. The exciton complexes scale exponentially $I \propto I_X^{\alpha}$, with a factor $\alpha > 1$. But in our case, at excitation intensities below 8.7 uW, the exciton and the trion peak show a sublinear behaviour, while the top induced peak shows a perfectly linear behaviour. The exciton shows an $\alpha \approx 0.58$ and the trion has an $\alpha \approx 0.95$. This is unexpected and such a intensity dependent behaviour of trions and excitons has, to my best knowledge, not been observed before in a WSe_2 monolayer.

Even more intriguing is the behaviour at incident powers above 8.7 uW. There, the PL intensity of the tip induced spectral feature abruptly drops and effectively vanishes for an excitation intensity of 17.8 uW. We can see an incident laser power dependent phase transition of the PL emission. In the high power regime the exciton and trion emission recovers and if we consider the slope between the recovered peak at 17.8 uW and the PL peak at the lowest power we obtain an alpha which is close to the expected value of $\alpha \approx 0.96$. The same consideration for the trion peak gives us an $\alpha \approx 1.15$ which agrees with reported exponents of other studies[36]. This measurement is

repeatable and the tip induced localized emission recovers when the excitation power is lowered again. So no degradation effects of the WSe_2 flake due to the high incident power are influencing the measurement.

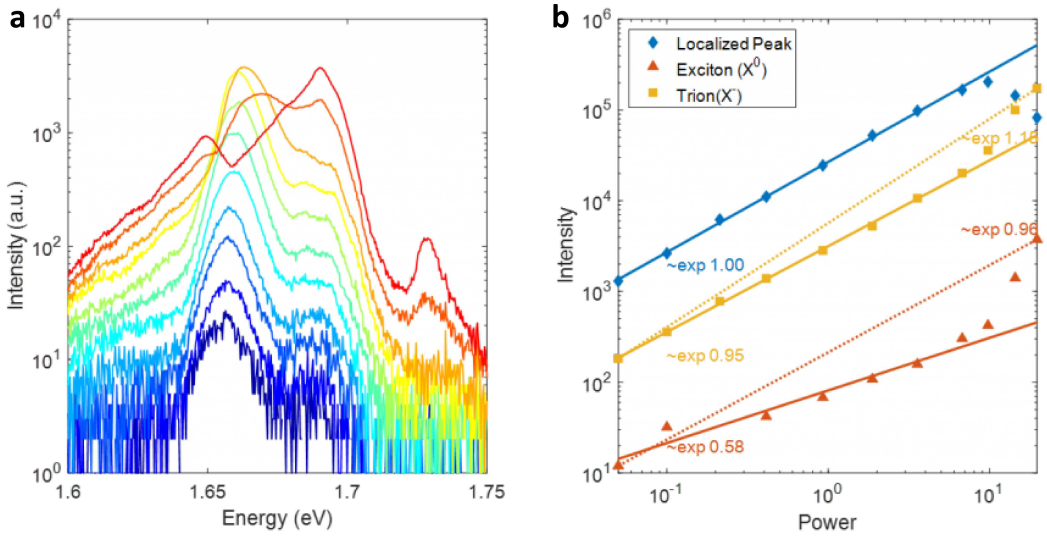

Figure 10: Exciation intensity dependence. **a**, Logarithmic plot of the PL spectrum for excitation powers (blue to red): 0.04 uW, 0.09 uW, 0.19 uW, 0.36 uW, 0.78 uW, 1.56 uW, 3.1 uW, 6.0 uW, 8.7 uW, 12.6 uW, 17.8 uW. **b**, Double logarithmic plot of the different peaks observed in the PL spectrum. The power scale is given in uW. Symbols: data points; Solid lines: fits of the low power region; Dashed lines: fits of the first and last data point.

5.3 Tip distance

Finally, we investigate how the tip distance influences the localized PL emission. Till now the tip was always in contact with the vdW stack. Now we retract the tip stepwise and measure the optical PL response. As before, we keep the tip voltage at V_{tip}10 V while keeping the backgate V_{bg}= 0 V. In Figure 11a we show a colormap of the PL intensity depending on the tip distance. The colormap shows that the tip induced peak is only existing when the tip is closer to the vdW stack than 200 nm. In this close proximity region a shift in energy of the tip induced peak is apparent. Which hints that the energy of the tip induced emission depends on the size of the band bending region in the WSe_2 flake. For a distance $>$ 200 nm, no tip induced emission line is visible. However, the negative trion peak intensity rises with the disappearance of the localized emission.

If the tip is further retracted the strongly pronounced negative trion peak is decreasing and around a micrometer in distance the tip influence is vanished. Figure 11b shows the PL spectra of the colormap in 11a. The localized emission peak (LP) and the negative trion (X^-) peak are fitted with a Lorentzian function, see Equation 1. The fitted parameters of the localized peak are shown Subfigures 11c-e and the fitted parameters of the negative trion are presented in Subfigures 11f-h. Notice the difference of the length scale of the distance for the Subfigures of the tip induced peak and the trion peak. Let us first look at the localized peak emission with the tip in close proximity (distance $<$ 200 nm). The energy of the localized peak (named peak position in Subfigure 11c), shows a linear dependence on tip distance. When the tip is in contact with the sample the tip

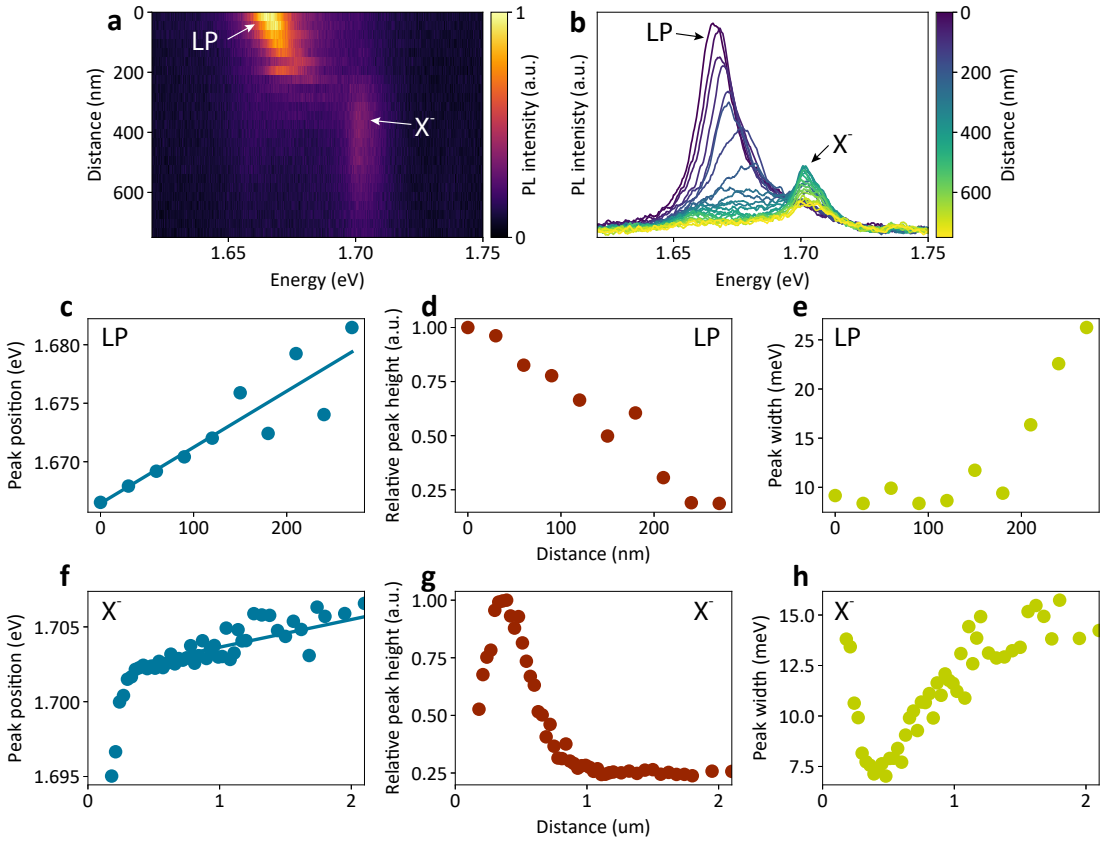

Figure 11: Tip distance dependence. **a**, PL intensity map with varying tip distance. A distance of 0 nm means that the AFM tip is in contact with the sample. **b** Waterfall plot of the PL intensity with varying distance. **c-e** Position, height and width of the localized peak (LP) obtained by fitting of the PL measurements. **f-h** Position, height and width of the trion (X^-) obtained by fitting of the PL measurements.

induced peak emits at 1.67 eV and has a gradient of $\nabla_{x_0} = 4.8 \times 10^{-2}$ meV/nm. The reduction of binding energy of the localized peak with increasing distance of the tip is probably due to a reduction of the band bending, which depends on the electric field strength. Since the electric field is reduced when the tip is retracted, the binding energy of the localized peak is reduced as well. The peak height is decreasing with tip distance, shown in Subfigure 11d, while the peak width is only changing during the transition from localized peak too free exciton emission, which happens around $\sim$ 200 nm, as can be seen in Subfigure 11e. The trion emission energy is also tuned by the tip distance, but the gradient is an order of magnitude smaller $\nabla_{x_0} = 1.8 \times 10^{-3}$ meV/nm, compared to the gradient of the localized peak. The trion peak intensity is highest when the localized peak just vanished and the decreases fast and converges to a constant value of approximately a quarter of the maximum peak intensity, when the peak is further than 1 um away. In contrast to the localized peak, the peak width is depending on the tip distance, and is reduced when the trion peak is more pronounced.

If we look at this measurements from the opposite side, a tip approach instead of a retraction, a charged AFM tip ($V_{tip} = 10$ V) starts to show it's influence when it is around 1 um away by

increasing the negative trion emission peak. When the distance is reduced to around 200 nm, the trion peak vanishes and a novel spectral feature appears which binding energy and PL intensity increases when the tip is getting closer to the WSe_2 flake.

5.4 Summary

Due to the large number of results and observations form our experiments we give here a structured overview of our insights about this tip induced PL emission:

- With a charged AFM tip in proximity of a grounded WSe_2 we are able to create a novel spectral PL feature at 1.67 eV which has a much stronger intensity than the free exciton and trion peaks.
- We can change the in-plane position of this localized emission with the position of the AFM tip.
- The localized emission is only appearing for positively charged tip voltages, and the onset of the tip induced emission depends on the backgate voltage and therefore onto the number of charge carriers in the sample.
- The backgate voltage controls the emission energy and we were able to tune the emission by ~ 14 meV. Also the emission intensity depends on the backgate voltage and therefore the number of charge carriers in the atomically thin semiconductor.
- The degree of polarization (DOP) of the PL emission is 0.37 for circularly polarized excitation and 0 for linear polarization, which hints to a charged excitonic complex as a source for the PL emission.
- PLE revealed that the PL emission of the localized peak is resonant with the free exciton and that the emission efficiency can be increased by a factor of 3.3, when the off and on resonant PL intensity is compared.
- Fluence dependent measurements shows that the localized peak intensity scales linearly with the excitation intensity, which is the same behaviour as the free exciton.
- When the sample is excited by a fluence greater than $\sim 20\,\mathrm{uW/um^2}$ the tip induced peak emission vanishes and the emission lines which are observed without a charged AFM tip (exciton, trion, localized excitons) appear again. This is a fluence dependent phase transition and is a novel behaviour for PL emission peaks in WSe_2.
- When the tip is retracted from the WSe_2 flake, first the localized emission binding energy is reduced before it vanished for a distance of ~ 200 nm.
- A tip-sample distance between 200 nm and 1 um, the negatively charged trion is pronounced, up to a factor of 4. Above a distance of 1 um, the influence of the charged tip is not longer observable.

6 Conclusion and outlook

In conclusion, we showed that a positively charged AFM tip introduces a novel spectral feature with a strong PL emission. We built an experimental setup, wrote software to control the experiment, and fabricated multiple samples in the course of this project. We conducted a comprehensive experimental study and characterized this localized spectral peak optically. We are able to control the peaks emission properties by electrical and optical means. However, the microscopic nature of this emission is not clear yet and is in need of a thorough theoretical study. Our tip induced PL emission shows a fundamentally different behaviours than the well studied free and localized exciton complexes.

Due to the novelty of this effect there are now a multitude of unexplored research directions to go for. One obvious direction is to go for smaller tip radii which would be possible by using sharper AFM tips or by using scanning tunneling microscopy (STM) tips which are mostly based on tungsten and can have atomically thin tips. Also magnetic AFM tips sound very promising since the magnetic flux at the tip would be extremely strong and the localization of the magnetic field could lead to novel optoelectronic effects. If the band bending localization could reach length scales of the exciton or trion radius, the formation of electrostatically confined quantum dots would be feasible. Such quantum dots could maybe form single photon emitters which are the basic building block for optical quantum computing and quantum communication. In regard to our built experimental setup it would be interesting to excite with a pulsed lasers to investigate at even higher fluence. Furthermore, pump probe experiments could give more information about the fundamental properties of this emission.

In the end this project was a great success and we were able to observe and investigate a novel tip induced PL emission. A theoretical investigation is now required to gain a microscopic understanding of the nature of this emission. Our investigation could be the starting point for many different tip induced and tip localized investigations in atomically thin crystals.

7 Acknowledgment

I am grateful to the Austrian Marshall Plan Foundation for giving me this opportunity to explore research avenues and making this valuable experience possible. I am indebted to Prof. Dirk Englund who gave me the opportunity to work in his research group and to Prof. Thomas Müller for his constant support. Furthermore, I want to thank Prof. Pablo Jarillo-Herrero who allowed us to use his facilities to fabricate the 2D material stacks. A special thanks goes to the members of the Quantum Photonics Laboratroy: Hyowon Moon, Christopher Panuski, Cheng Peng, Jordan Goldstein, Mihika Prabhu, Hugo Larocque, Liane Bernstein, Michael Walsh, Eric Bersin, Lorenzo De Santis, and Mikkel Heuck, who helped me in many ways pursuing this project and made my stay a really pleasurable experience. I would also like to take this opportunity to thank all the members of the Graphenelabs and THz Labs groups at the TU Vienna, and the Research Laboratory of Electronics, Massachusetts Institute of Technology, for making all the transitions seamless.

Bibliography

1. Mak, K. F., Lee, C., Hone, J., Shan, J. & Heinz, T. F. Atomically thin MoS 2: a new direct-gap semiconductor. *Physical review letters* **105,** 136805 (2010).
2. Cao, T., Wang, G., Han, W., Ye, H., Zhu, C., Shi, J., Niu, Q., Tan, P., Wang, E., Liu, B., *et al.* Valley-selective circular dichroism of monolayer molybdenum disulphide. *Nature communications* **3,** 1–5 (2012).
3. Xiao, D., Liu, G.-B., Feng, W., Xu, X. & Yao, W. Coupled spin and valley physics in monolayers of MoS 2 and other group-VI dichalcogenides. *Physical review letters* **108,** 196802 (2012).
4. Mak, K. F., He, K., Shan, J. & Heinz, T. F. Control of valley polarization in monolayer MoS 2 by optical helicity. *Nature nanotechnology* **7,** 494–498 (2012).
5. Sallen, G, Bouet, L, Marie, X, Wang, G, Zhu, C., Han, W., Lu, Y, Tan, P., Amand, T, Liu, B., *et al.* Robust optical emission polarization in MoS 2 monolayers through selective valley excitation. *Physical Review B* **86,** 081301 (2012).
6. Zeng, H., Dai, J., Yao, W., Xiao, D. & Cui, X. Valley polarization in MoS 2 monolayers by optical pumping. *Nature nanotechnology* **7,** 490–493 (2012).
7. Kormányos, A., Burkard, G., Gmitra, M., Fabian, J., Zólyomi, V., Drummond, N. D. & Fal'ko, V. k· p theory for two-dimensional transition metal dichalcogenide semiconductors. *2D Materials* **2,** 022001 (2015).
8. Molas, M. R., Faugeras, C., Slobodeniuk, A., Nogajewski, K., Bartos, M., Basko, D. & Potemski, M. Brightening of dark excitons in monolayers of semiconducting transition metal dichalcogenides. *2D Materials* **4,** 021003 (2017).
9. Zhang, X.-X., Cao, T., Lu, Z., Lin, Y.-C., Zhang, F., Wang, Y., Li, Z., Hone, J. C., Robinson, J. A., Smirnov, D., *et al.* Magnetic brightening and control of dark excitons in monolayer WSe 2. *Nature nanotechnology* **12,** 883 (2017).
10. Zhou, Y., Scuri, G., Wild, D. S., High, A. A., Dibos, A., Jauregui, L. A., Shu, C., De Greve, K., Pistunova, K., Joe, A. Y., *et al.* Probing dark excitons in atomically thin semiconductors via near-field coupling to surface plasmon polaritons. *Nature nanotechnology* **12,** 856 (2017).
11. Tonndorf, P., Schmidt, R., Schneider, R., Kern, J., Buscema, M., Steele, G. A., Castellanos-Gomez, A., van der Zant, H. S., de Vasconcellos, S. M. & Bratschitsch, R. Single-photon emission from localized excitons in an atomically thin semiconductor. *Optica* **2,** 347–352 (2015).
12. Srivastava, A., Sidler, M., Allain, A. V., Lembke, D. S., Kis, A. & Imamoğlu, A. Optically active quantum dots in monolayer WSe 2. *Nature nanotechnology* **10,** 491 (2015).
13. He, Y.-M., Clark, G., Schaibley, J. R., He, Y., Chen, M.-C., Wei, Y.-J., Ding, X., Zhang, Q., Yao, W., Xu, X., *et al.* Single quantum emitters in monolayer semiconductors. *Nature nanotechnology* **10,** 497–502 (2015).
14. Koperski, M, Nogajewski, K, Arora, A, Cherkez, V, Mallet, P, Veuillen, J.-Y., Marcus, J, Kossacki, P & Potemski, M. Single photon emitters in exfoliated WSe 2 structures. *Nature nanotechnology* **10,** 503 (2015).
15. Chakraborty, C., Kinnischtzke, L., Goodfellow, K. M., Beams, R. & Vamivakas, A. N. Voltage-controlled quantum light from an atomically thin semiconductor. *Nature nanotechnology* **10,** 507 (2015).

16. He, K., Kumar, N., Zhao, L., Wang, Z., Mak, K. F., Zhao, H. & Shan, J. Tightly bound excitons in monolayer WSe 2. *Physical review letters* **113,** 026803 (2014).

17. Mitioglu, A., Plochocka, P, Granados del Aguila, Á, Christianen, P., Deligeorgis, G, Anghel, S, Kulyuk, L & Maude, D. Optical investigation of monolayer and bulk tungsten diselenide (WSe2) in high magnetic fields. *Nano letters* **15,** 4387–4392 (2015).

18. Berkelbach, T. C., Hybertsen, M. S. & Reichman, D. R. Theory of neutral and charged excitons in monolayer transition metal dichalcogenides. *Physical Review B* **88,** 045318 (2013).

19. You, Y., Zhang, X.-X., Berkelbach, T. C., Hybertsen, M. S., Reichman, D. R. & Heinz, T. F. Observation of biexcitons in monolayer WSe 2. *Nature Physics* **11,** 477–481 (2015).

20. Ye, Z., Waldecker, L., Ma, E. Y., Rhodes, D., Antony, A., Kim, B., Zhang, X.-X., Deng, M., Jiang, Y., Lu, Z., *et al.* Efficient generation of neutral and charged biexcitons in encapsulated WSe 2 monolayers. *Nature communications* **9,** 1–6 (2018).

21. Li, Z., Wang, T., Lu, Z., Jin, C., Chen, Y., Meng, Y., Lian, Z., Taniguchi, T., Watanabe, K., Zhang, S., *et al.* Revealing the biexciton and trion-exciton complexes in BN encapsulated WSe 2. *Nature communications* **9,** 1–7 (2018).

22. Barbone, M., Montblanch, A. R.-P., Kara, D. M., Palacios-Berraquero, C., Cadore, A. R., De Fazio, D., Pingault, B., Mostaani, E., Li, H., Chen, B., *et al.* Charge-tuneable biexciton complexes in monolayer WSe 2. *Nature communications* **9,** 1–6 (2018).

23. Chen, S.-Y., Goldstein, T., Taniguchi, T., Watanabe, K. & Yan, J. Coulomb-bound four-and five-particle intervalley states in an atomically-thin semiconductor. *Nature communications* **9,** 1–8 (2018).

24. Kim, J., Wake, D. & Wolfe, J. Thermodynamics of biexcitons in a GaAs quantum well. *Physical Review B* **50,** 15099 (1994).

25. Birkedal, D., Singh, J., Lyssenko, V., Erland, J & Hvam, J. M. Binding of quasi-two-dimensional biexcitons. *Physical review letters* **76,** 672 (1996).

26. Phillips, R., Lovering, D., Denton, G. & Smith, G. Biexciton creation and recombination in a GaAs quantum well. *Physical Review B* **45,** 4308 (1992).

27. Jones, A. M., Yu, H., Ghimire, N. J., Wu, S., Aivazian, G., Ross, J. S., Zhao, B., Yan, J., Mandrus, D. G., Xiao, D., *et al.* Optical generation of excitonic valley coherence in monolayer WSe2. *Nature nanotechnology* **8,** 634 (2013).

28. Chakraborty, C., Mukherjee, A., Qiu, L. & Vamivakas, A. N. Electrically tunable valley polarization and valley coherence in monolayer WSe 2 embedded in a van der Waals heterostructure. *Optical Materials Express* **9,** 1479–1487 (2019).

29. Weimer, M, Kramar, J & Baldeschwieler, J. Band bending and the apparent barrier height in scanning tunneling microscopy. *Physical Review B* **39,** 5572 (1989).

30. Dombrowski, R, Steinebach, C., Wittneven, C., Morgenstern, M & Wiesendanger, R. Tip-induced band bending by scanning tunneling spectroscopy of the states of the tip-induced quantum dot on InAs (110). *Physical Review B* **59,** 8043 (1999).

31. Kemerink, M., Sauthoff, K, Koenraad, P., Gerritsen, J., van Kempen, H, Fomin, V., Wolter, J. & Devreese, J. Optical properties of a tip-induced quantum dot. *Applied Physics A* **72,** S239–S242 (2001).

32. Ekardt, W, Lösch, K & Bimberg, D. Determination of the analytical and the nonanalytical part of the exchange interaction of InP and GaAs from polariton spectra in intermediate magnetic fields. *Physical Review B* **20,** 3303 (1979).

33. Tong, H & Wu, M. Theory of excitons in cubic III-V semiconductor GaAs, InAs and GaN quantum dots: fine structure and spin relaxation. *Physical Review B* **83,** 235323 (2011).

34. Hohenester, U. Optical properties of semiconductor nanostructures: decoherence versus quantum control. *arXiv preprint cond-mat/0406346* (2004).

35. Gorbachev, R. V., Riaz, I., Nair, R. R., Jalil, R., Britnell, L., Belle, B. D., Hill, E. W., Novoselov, K. S., Watanabe, K., Taniguchi, T., *et al.* Hunting for monolayer boron nitride: optical and Raman signatures. *Small* **7,** 465–468 (2011).

36. Paur, M., Molina-Mendoza, A. J., Bratschitsch, R., Watanabe, K., Taniguchi, T. & Mueller, T. Electroluminescence from multi-particle exciton complexes in transition metal dichalcogenide semiconductors. *Nature communications* **10,** 1–7 (2019).